Advanced Electron Microscopy Techniques on Semiconductor Nanowires: from Atomic Density of States Analysis to 3D Reconstruction Models

Sònia Conesa-Boj[1], Sònia Estradé[1], Josep M. Rebled[1], Joan D. Prades[1],
A. Cirera[1], Joan R. Morante[1,2], Francesca Peiró[1], and Jordi Arbiol[1,3,*]
[1]Dept. d'Electrònica, Universitat de Barcelona
[2]IREC, Catalonia Institute for Energy Research
[3]ICREA Research Professor at Institut de Ciència de Materials de Barcelona, CSIC
Spain

1. Introduction

Technology at the nanoscale has become one of the main scientific world challenges as new quantum physical effects appear and can be modulated at will (Kastner, 1992). Superconductors, materials for spintronics, electronics, optoelectronics, chemical sensing, and new generations of functionalized materials are taking advantage of the low dimensionality, improving their properties and opening a new range of applications (De Franceschi et al., 2003; Samuelson et al., 2004; Fischer et al., 2006; Pettersson et al., 2006; Wang et al., 2006; Hernández-Ramírez et al., 2007; Qin et al., 2007; Appenzeller et al., 2008; Boukai et al., 2008; Hochbaum et al., 2008; Wang et al., 2008; Colombo et al., 2009; Thunick et al., 2009). These new materials for future applications are being synthesized at the nanoscale (ultrathin layers, nanoparticles, nanowires or nanotubes functionalized). Among all these new materials, one-dimensional (1D) nanostructures such as nanowires, are one of the most used and promising morphologies (Lieber, 2003; Yang, 2005; Thelander et al., 2006; Lieber & Wang, 2007). Groups all around the world in the area of materials science, physics, chemistry and biology work in close collaboration with nanoscopy tools as there is a critical need for the structural, chemical and morphological characterization of the synthesized nanostructures at atomic scale in order to correlate these results with the physical and chemical properties and functionalities they present. In order to obtain an accurate control and understanding of these new materials properties, it is essential to access their structure and chemistry at atomic scale. Electron Microscopy and more precisely (scanning) transmission electron microscopy ((S)TEM) and electron spectroscopy related techniques (also known as electron nanoscopies) have thus a preeminent role in advanced materials science. Recent developments in electron microscopy, such as aberration correctors and monochromators are allowing us to reach sub-angstrom and sub-eV, spatial and energy resolutions, respectively. In addition to these advances, the possibility to obtain 3D models of our nanostructures by means of electron tomography, have shown that Electron Microscopy related techniques are the most promising to fully characterize complex

nanostructures. In the present chapter we will show how advanced electron microscopy techniques can be applied to obtain a deeper characterization of complex structures in semiconductor nanowires. The chapter will be distributed in two parts: in the first one, we will show the advantages of using aberration-corrected STEM and monochromated electron energy loss spectroscopy (EELS) in order to deeply characterize 1-D nanostructures at atomic scale. As an advanced example of how these techniques can improve Nanowire characterization, we will show how they can allow the local analysis of the atomic scale modifications in the local density of states that occur in a complex system in which high Mg-doping induces formation of transversal twin defects (perpendicular to the growth axis) on GaN Nanowires (NWs). Formation of these defects generates local structural phase changes, thus implying a different optoelectronic behavior of the nanowires, induced by the local change in the material bandgap. The considered techniques can allow measuring the bandgap exactly in every atomic column, thus leading to a complete characterization. In the second part of the chapter, we will focus on how 3D reconstruction of 1D nanostructures by means of electron tomography can improve the morphological characterization at the nanoscale. As advanced examples of this part, we will show how to obtain 3D models of complex coaxial nanowire heterostructures.

2. Aberration-corrected scanning transmission electron microscopy and monochromated electron energy loss spectroscopy

2.1 State of the art

Nowadays, given the eventual reduction in scale of the challenges at hand and the progressive instrumental advances that have taken place in microscopy in general and in EELS in particular, EELS has become one of the most crucial tool in materials science and even the life sciences (Calvert et al., 2005; Pan et al., 2009). As EELS is performed in the Transmission Electron Microscope (TEM), it benefits from the very high spatial resolution that can be achieved with electron optics, which can focus the electron beam to form a subnanometric probe. In particular, if a field emission gun is used, sufficient current can be obtained for a 1 nm probe. Within aberration-corrected instruments, this figure can be reduced to 0.1 nm. In addition, EELS can be easily combined with structural information as obtained from the TEM imaging and diffraction modes, and even with complementary X-ray energy-dispersive spectroscopy (EDXS) if needed. There is a fundamental limit to the minimum lateral resolution that can be achieved by EELS, irrespective of the electron optics. This limit is given by the delocalisation produced in inelastic scattering, and depends on the energy loss (the lower the loss, the greater the delocalisation) (Egerton, 1996). Yet, fortunately, this limit does not prevent from getting EELS signal from single atom columns at core-loss (Allen, 2003) or subnanometric resolution in low-loss experiments (Grogger, 2005). With the recent advances in instrumentation (spherical aberration correctors, electron monochromators, new energy filters and CCD detectors) EELS experiments can now be performed with a spatial resolution well below 0.1 nm and an energy resolution better than 0.1 eV. One of the instrumental highlights in the history of TEM is the recent introduction of systems to compensate for spherical and even chromatic aberrations (Haider et al., 1998; Batson et al., 2002). Using aberration corrected microscopy, an electron probe smaller than 1 Å can be achieved, which allows imaging of single atoms, clusters of a few atoms, and atomic columns. A multipole corrector built into the illumination system of a STEM increases the image resolution and allows more current to be focused in a given probe. This

is of great importance for spectroscopy, as both lateral resolution and signal-to-noise ratio are enhanced. If EELS presents a lower energy resolution when compared to other spectroscopies as XAS, the limitation does not lie in the capabilities of the spectrometers, but in the energy width of the electron source. This energy dispersion is typically 1–2 eV for a thermionic source, 0.5–1 eV for a Schottky or hot field-emission tip and around 0.3-0.35 eV for a cold field-emission tip. For comparison, synchrotron X-ray sources and beam-line spectrometers commonly provide a resolution below 0.1 eV for absorption spectroscopy, and even below 1 meV in certain cases (Egerton, 2003). In order to reduce the source energy spread, monochromators have been recently introduced. Nowadays, the monocromators yield a beam current in the order of several 100 pA (Tsuno, 2000; Egerton, 2003; Sigle, 2005). In particular, and due to all these achievements, HREELS associated to STEM in HRHAADF mode, can be used to solve the local electronic properties in nanostructured materials. In this way, bulk plasmon peak position can be used as an indirect compositional measure, and has been extensively used as a local chemical characterization tool, especially in the case of semiconductors. It can be primarily used as an identification tag for determining which compound is there at a given region of the studied specimen (Topuria et al., 2003; Irrera et al., 2005). As the plasmon peak position depends on the lattice parameter (as well as the bandgap energy and the dielectric constant) it can also give an indirect measure of structural properties (Shen et al., 2000; Sanchez et al., 2006). The need for characterization techniques that provide precise information regarding the bandgap and general optical properties at high spatial resolution seems to be out of question, given the scaling down that has taken place in the field of materials science and the rapidly widening use of nanostructures. In this sense, standard optical techniques such as vacuum ultra-violet spectroscopy do not provide the spatial resolution required to probe a material on the nanometer scale. Low-loss EELS seems to be a most fitting technique for the local characterization of optoelectronic properties at the nanoscale. For insulators or semiconductors with a sufficiently wide bandgap (that can be less than 1 eV using a monochromated STEM (Erni & Browning, 2005)), interband transitions can be observed in the EELS spectrum. It is possible to identify through EELS the bandgap energy of given nanostructures (Kuykendall et al., 2007; Arenal et al., 2008; Iakoubovskii et al., 2008). It is also possible to assess the existence of localized states within the bandpgap, which may be due to the presence of dislocations or other kinds of defects, for instance (Batson et al., 1986; Xin et al., 2000), which create new energy levels in the local DOS.

2.2 Particular case: Local electronic properties of Mg doped GaN NWs

In recent years much attention has been focused on the growth of quasi-one-dimensional (1D) nanostructures for the controlled fabrication of nanodevices (Arbiol et al., 2002; Hernandez-Ramirez et al., 2007; Hochbaum et al., 2008; Nesbitt, 2007; Stern et al., 2007). In particular, III-nitrides (InN, GaN, AlN and their alloys) have shown promising properties. Their direct band gap can be controlled from 0.7 eV (InN) to 3.4 eV (GaN) and to the deep UV spectral range of 6.0 eV (AlN). This makes them excellent candidates for the fabrication of heterostructures for optoelectronic applications, such as light emitting diodes, laser diodes, or quantum well infrared photodetectors as well as high electron mobility transistors. The synthesis of p-type 1D nanostructures based on these III-nitrides is still a challenging topic. To exploit these material properties also in nanoscaled devices, catalyst-induced processes like the vapour liquid solid (VLS) mechanism (Wagner & Ellis, 1964;

Morral et al., 2007), using metal droplets like Au, Ni (Chen et al., 2001; Kim et al., 2003), or Fe (Chen et al., 2001) as catalysts have been developed for the growth of GaN nanorods (NRs) or nanowires (NWs) with vertical orientation with respect to the substrate, with horizontal orientation, or as free structures. GaN NWs grown by laser assisted catalytic growth have been reported and heterodiodes have been realized by deposition of n-type GaN NWs on p-type Si substrates (Huang et al., 2002). However, for the integration of more complex structures such as p–n junctions or quantum wells, and in order to avoid the negative effects of catalysts in group III–V NRs or NWs, molecular beam epitaxy (MBE) is the growth method of choice (Calleja et al., 2000; Colombo et al. 2008; Morral et al., 2008b). As mentioned above, for the realization of nanoelectronic devices doping is one of the most important issues. In the case of Mg doped (p-type) GaN NRs and NWs, only a few studies have been devoted to analyze their optoelectronic (Furtmayr et al., 2008a; Furtmayr et al., 2008b; Park et al., 2006a; Zhong et al., 2003; Lai et al., 2006; Pal et al., 2006), transport, and electronic properties (Cheng et al., 2003; Zhong et al., 2003; Park et al., 2006b). Some of these works have provided limited information on the morphology (Park et al., 2006a) and crystal structure (Cheng et al., 2003; Zhong et al., 2003; Cimpoiasu et al., 2006) of the Mg doped GaN NRs and NWs. In addition, the analysis of GaN NWs as a model system for single crystals with a very low defect density can also contribute to solving some of the still existing technological problems of p-type doping of GaN with Mg in general. To this end, in the following we will show how combination of atomically resolved high resolution electron energy loss (EEL) measurements with specific *ab-initio* calculations can be a useful way to demonstrate that the presence of Mg atoms during the growth of GaN nanowires results in direct structural and morphological modifications with significant effects on the local electronic structure.

2.3 Experimental details: Growth method

Gallium nitride nanowires were grown using plasma assisted molecular beam epitaxy (PAMBE). Nitrogen radicals were supplied by an Oxford Applied Research RF-plasma source whereas for Ga and Mg thermal effusion cells were used. Low resistivity n-type Si(111) substrates were etched in 5% hydrofluoric acid for 10 s to remove the surface oxide layer prior to transfer into the load lock chamber. For all samples a substrate temperature of 790 $^{\circ}$C, a nitrogen pressure of 2.7×10^{-5} mbar and a Ga beam equivalent pressure (BEP) of 3.3×10^{-7} mbar was used. The substrates were exposed to the nitrogen plasma at a temperature of 790 $^{\circ}$C for 2 min directly before GaN growth. For the magnesium doped samples the Mg effusion cell temperature (TMg) was varied between 205 $^{\circ}$C and 355 $^{\circ}$C, corresponding to a BEP of 1×10^{-11} mbar to 2×10^{-8} mbar, respectively. Growth duration was 90 min unless mentioned otherwise. Samples were grown by Florian Furtmayr, Christoph Stark, Martin Stutzmann and Martin Eickhoff (Walter-Schottky-Institut, Technische Universität München) and Andreas Laufer (I Physikalisches Institut, Justus-Liebig-Universität).

2.4 Transmission electron microscopy characterization

In order to analyze the influence of the Mg doping on the atomic structure of the Mg NWs, selected area electron diffraction (SAED) patterns were obtained on several samples, prepared in XTEM geometry (Fig. 1. SAED analysis). Fig. 1.(a) shows a bright field STEM (BFSTEM) general view of the undoped GaN NWs. Its corresponding SAED pattern is displayed in Fig. 1.(b).
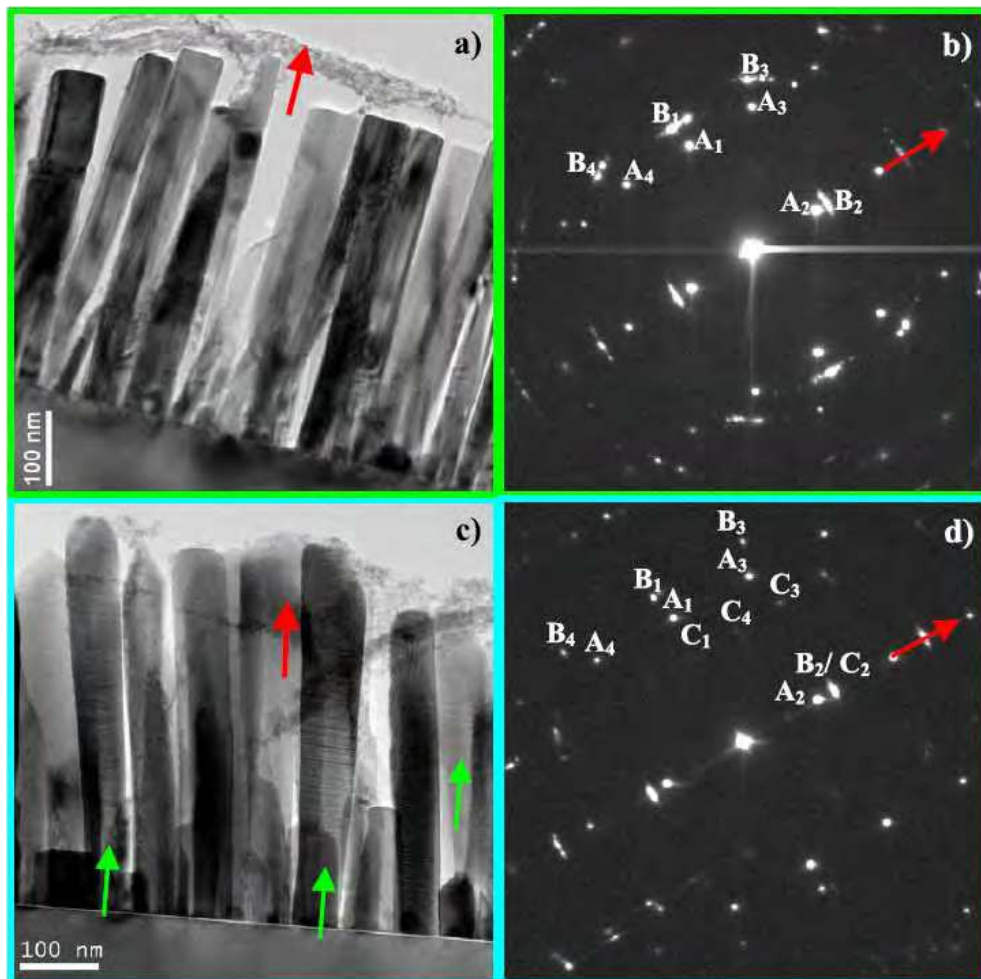
Fig. 1. SAED analysis

On the other hand, Fig. 1.(c) shows a BFSTEM general view of the highly Mg doped (TMg = 355 °C) GaN NWs. Some of the NWs present twin defects (marked with green arrows). In this case, Fig. 1.(d) displays its SAED pattern. A new crystal orientation appears in this case, that has been related to the twinned NWs (spots labelled as C). Top arrows (red) are pointing to the same equivalent growth direction in SAED patterns and BFSTEM micrographs. After this analysis (see the corresponding indexation in Table 1. SAED patterns indexation) it was observed that GaN NWs follow a preferential epitaxial relationship versus the Si substrate, namely: (0001)[0-110] GaN // (111)[-1-12] Si (Arbiol et al., 2009). Undoped GaN NWs appear to be defect-free, whilst Mg doped samples present some NWs with twin (T) defects along the growth axis, as shown in Fig. 1.(a) and (b) -some twinned NWs have been marked with green arrows in Fig. 1.(c). When a SAED pattern of a NW region populated with few twinned NWs is obtained, a new orientation relationship

superimposed to the one found for undoped samples can be observed. As shown in Fig. 1.(d), the new spots (indexed in Table 1. SAED patterns indexation), labeled as C_n, are rather weak. The presence of these weak spots can be attributed to the presence of Ts in the NWs. The new epitaxial relationship which is found is: (0001)[1-210]GaN // (111)[-1-12]Si. The twinned NWs still grow along the [0001] direction; however, they are rotated 30° along the growth axis with respect to the non-twinned NWs.

Spot #	d (nm)	(deg) versus spot A_1	Indexation
A1	1.92	—	(2-20)
A2	3.13	90	(111)
A3	1.64	31	(3-11)
A4	1.64	31	(1-3-1)
Zone axis: [-1-12] Si			

Spot #	d (nm)	(deg) versus spot B_1	Indexation
B1	1.55	—	(-2110)
B2	2.59	90	(0002)
B3	1.30	32	(-2112)
B4	1.30	32	(-211-2)
Zone axis: [0-110] GaN			

Spot #	d (nm)	(deg) versus spot C_1	Indexation
C1	2.76	—	(-1010)
C2	2.59	90	(0002)
C3	1.89	43	(-1012)
C4	2.44	62	(-1011)
Zone axis: [1-210] GaN			

Table 1. SAED patterns indexation

The density of twins dramatically increases with increasing Mg concentration and, thus, the formation of twins can be directly correlated to the increasing presence of Mg. Twin defects along the growth axis have been commonly observed in some other one-dimensional semiconductor nanostructures such as in III–V NWs (Huang et al., 2002; Mikkelsen et al., 2004; Johansson et al., 2006; Davidson et al., 2007; Karlsson et al., 2007; Arbiol et al., 2009), or even in Si NWs (Arbiol et al., 2007; Arbiol et al., 2008b).

High resolution TEM (HRTEM) analysis (Fig. 2. HRTEM analysis of the highly Mg-doped GaN NWs) confirms that NWs with Ts grow in the (0002)[1-210]GaN // (111)[-1-12]Si orientation and are rotated 30° from the defect-free NWs. As shown in Fig. 2.(e), red arrows are pointing towards GaN(0001) wurtzite planes, while the cyan ones are pointing to the GaN twinned planes (in particular to a triple-twin region). As observed, the stacking of the planes is different in the twinned regions. On the other hand, an amorphous layer between the substrate and the GaN NW is apparent in Fig. 2.(a). Core-loss EELS quantification along the interface was carried out to find out the chemical nature of this amorphous layer. As Si
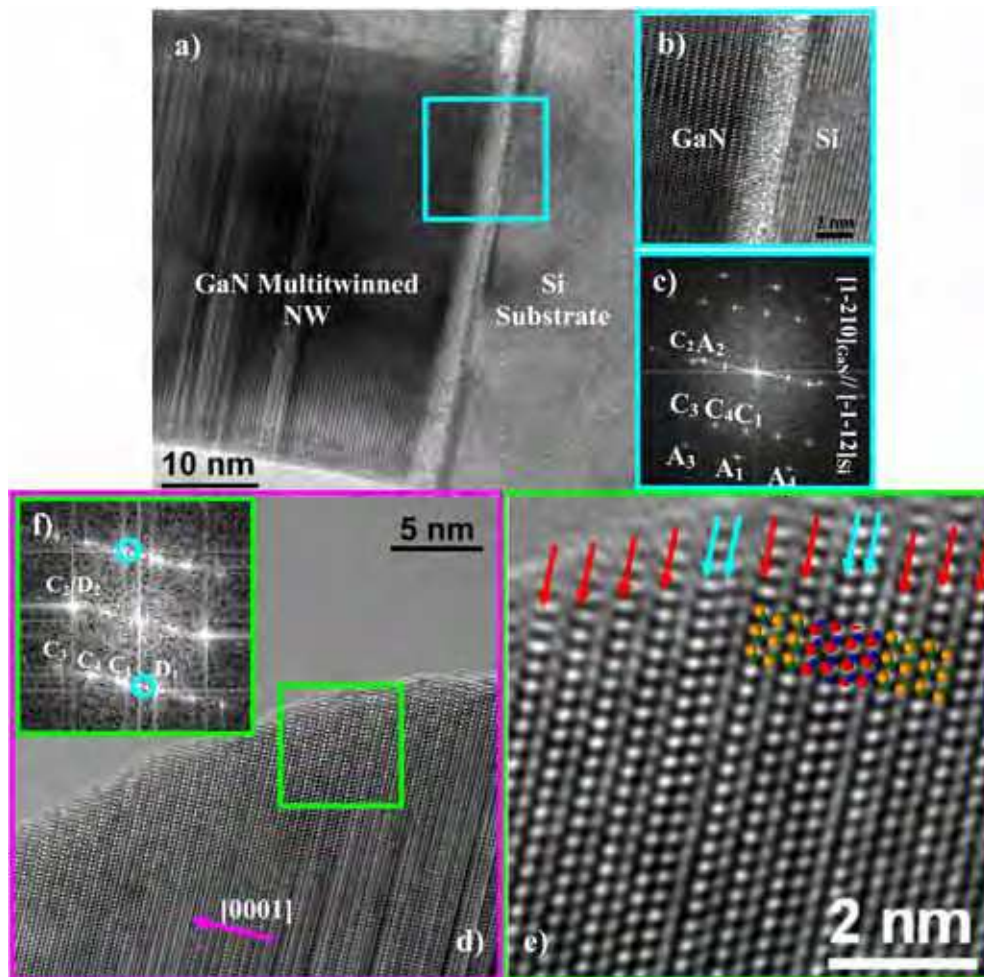
Fig. 2. HRTEM analysis of the highly Mg-doped GaN NWs

$L_{2,3}$ and Ga $M_{2,3}$ edges overlap, quantification was not carried out in the usual manner (computing background subtracted integrated signals for each element, sigma correcting them and dividing them by each other), but rather treating the overlapping region as a linear combination of the Si and Ga edges. This way, it was found that the amorphous layer contained 50 ± 5 % of Si, 50 ± 5 % of N and no Ga (Fig. 3. GaN/Si interface EELS analysis). This Si nitride layer was very likely created during the nitridation process that occurred during the first growth steps. A scheme of the twin formation is also shown (Fig. 4. Twin formation scheme). Fig. 4.(a) represents the conventional GaN wurtzite (WZ) structure, while in Fig. 4.(c) the formation of a single twin, equivalent to a 180° rotation in the WZ structure around the [0001] growth axis, is shown. It is important to point out that the consecutive stacking of [0001] axial twins leads to the formation of the GaN zinc-blende (ZB) structure, which is cubic instead of hexagonal (Fig. 4.(b) for a scheme of the GaN ZB structure).
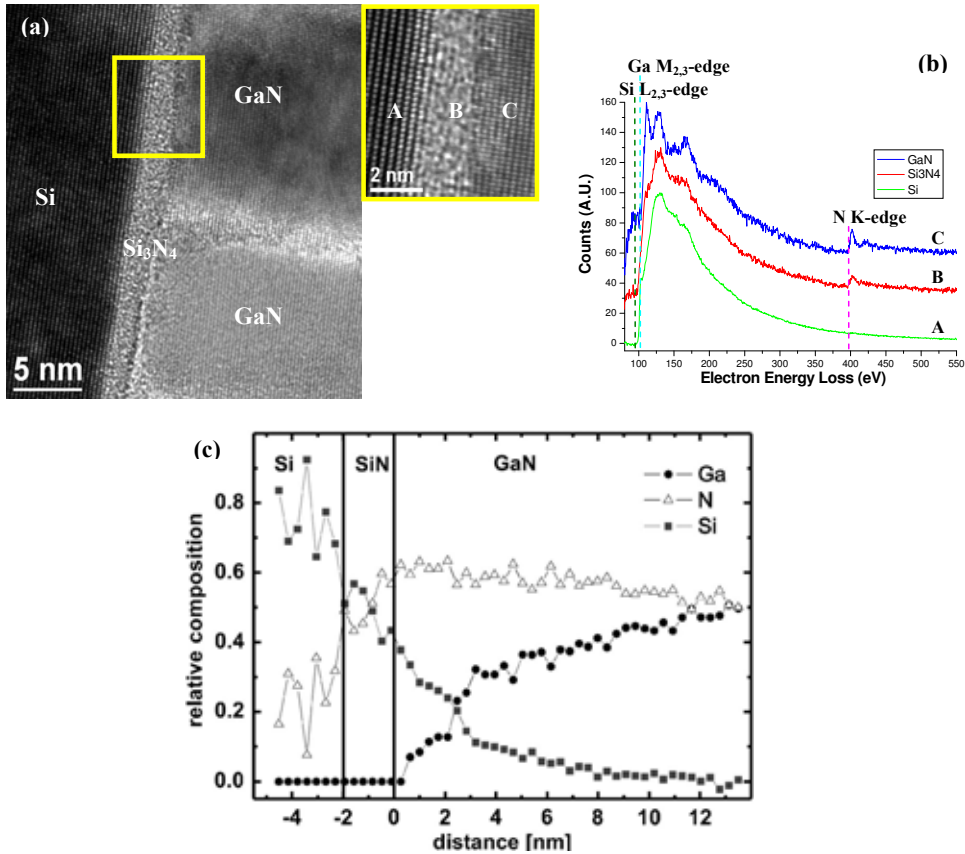
Fig. 3. GaN/Si interface EELS analysis. For Fig. 3.(c) see (Arbiol et al., 2008b).

In particular, it is displayed how a triple-twin creates a three-cell ZB domain (Figs. 2.(e) & 4.(e)). In this way, in the power spectrum shown in Fig. 2.(f), the D1 spot corresponds to the (-11-1) GaN ZB plane, while the D2 spot is the (111) plane. The appearance of alternating wurtzite and zinc-blende structures due to the presence of twins has been widely reported for III–V NWs (Banerjee et al., 2006; Ihn et al., 2006; Arbiol et al., 2008b) and the change of crystal phases in 1D nanostructures due to twinning is a widespread phenomenon in several materials (Arbiol et al., 2008a). In addition, the formation of wurtzite and zinc-blende heterostructures in a chemically homogeneous nanowire material is a hot scientific topic as it is opening up new possibilities for band-structure engineering (Algra et al., 2008; Arbiol et al., 2008b; Bao et al., 2008). These heterostructures can have dramatic implications on the electronic properties of the NWs, as a change in the crystal structure also implies a variation in the density of states and thus on the carrier transition energy.

In the present case, due to the different band gap, the resulting inclusion of ZB GaN in the WZ GaN NW creates quantum well regions along the NW axis. In a recent work (Bao et al., 2008), it was shown how the presence of twinned planes between WZ quantum domains in InP NWs (they attributed it to WZ–ZB alternance) could influence their photoluminescence properties.

In their case, the excitation power dependent blueshift of the observed photoluminescence could be explained in terms of the predicted staggered band alignment of the rotationally twinned ZB/WZ InP heterostructure and of the concomitant diagonal transitions between localized electron and hole states responsible for radiative recombination.
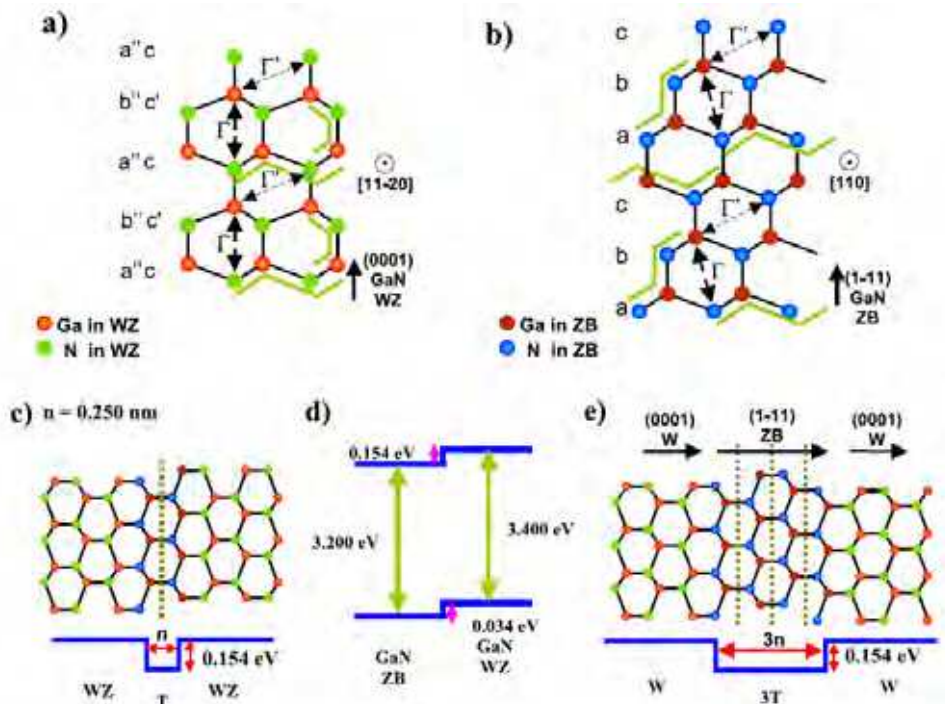

Fig. 4. Twin formation scheme

2.5 Local optical properties addressed through EELS:
Plasmon position and structural considerations
Low-loss spectra were acquired along the doped NWs using a GIF2001 spectrometer coupled to a JEM2010F microscope. The plasmon position was found to remain constant along the NW. Now, the plasmon position depends on bandgap, but it also depends on other factors that may cancel out. In particular, it is possible to assume that plasmon position depends on the composition and the distance to the first neighboring atom, which are the same for WZ and ZB regions in the NWs, so that even if the bandgap changes, the plasmon energy remains the same. In other words, the unchanging plasmon position does not need to correspond to unchanging bandgap energy. This affirmation will be further sustained by ab-initio simulations in the following section. On the other hand, it is clear that EELS spectra with a better energy resolution are needed to access the bandgap energy.

Bandgap estimation
Aberration-corrected STEM, and EELS spectra with a 0.3 energy resolution were used to move one step further and locally analyze the local density of states at the atomic scale that

occur in the interface between the triple-twin (3T) planes (ZB) and the WZ GaN heterostructure. Experiments were performed on a dedicated VG HB 501 STEM retrofitted with a Nion quadrupole–octupole corrector (SuperSTEM 1) at Daresbury (Arbiol et al., 2009). Cs-corrected HRHAADF STEM micrographs, where the displayed bright spots directly correspond to the actual atomic positions, corroborate the proposed structural model for the 3T domains (Fig. 5. High-resolution HAADF twin domain and local HREELS Bandgap analysis). EEL spectra maps of the NWs were obtained with a zero loss peak (ZLP) energy FWHM of 0.3 eV and a probe size of about 0.1 nm. The much reduced probe size allowed us to obtain several EEL spectra in the direction perpendicular to the NW growth direction for wurtzite and 3T planes (see square blue and red marks in Fig. 5.(a) for the EELS selected areas). Then, the spectra obtained at the exact atomic positions with respect to the wurtzite and the 3T regions were processed and analyzed. These spectra are displayed in Fig. 5.(b). It is generally accepted that the ZLP shape is Gaussian (Egerton, 1996), and thus that it contributes to the low-loss signal as $A \exp(-rx^2)$, where x is the energy loss. In the present work, it was subtracted from the low-loss region by fitting an $A \exp(-rx^2)$ function to the positive tail of the ZLP. The resulting spectra (Fig. 5.(b)) show several interesting features –before analyzing the low-loss spectra, it should yet be noticed that the peak observed at about 24 eV is in fact the Ga 3d transition. The obtained band gap is found to be higher for the WZ region (measured to be 3.4 eV) than for the 3T region (measured to be 3.2 eV). The values are comparable to the band gap measurements for WZ and ZB phases obtained by EELS in literature (Bangert et al., 1998; Lazar et al., 2003) but, interestingly, lower than the values obtained using other techniques. On the other hand, features B and C in Fig. 5.(b) are found at higher energies for zinc-blende GaN than for wurtzite GaN. These peaks were expected, from first principles calculations (Gavrilenko & Wu, 2000), to arise from transitions from the three upper valence bands to the third and fourth conduction bands (B), and from the same bands to the fifth and upper conduction bands (C), occurring at higher energies for ZB GaN than for WZ GaN. Finally, the higher intensity of the EELS spectrum in the region <15 eV and the broadening of the plasmon peak for the faulty region can be related to the occurrence of surface modes (Egerton, 1996; Erni & Browning, 2005) corresponding to the WZ–ZB–WZ interface (Fig. 5.(b)). Specific ab initio simulations of the EELS spectra of pristine bulk wurtzite and defective bulk wurtzite (triply-twinned inclusion) were carried out (Figs. 5.(c) & (e)) in order to corroborate the origin of these experimental features. Ab initio calculations were carried out using the SIESTA (Soler et al., 2002) code, which combines density functional theory (DFT), normconserving pseudopotentials, and local basis set functions.

We used the generalized gradient approximations (GGAs) with the Perdew, Burke, and Ernzerhof (PBE) parameterization (Perdew et al., 1996). For Ga and N atoms, the double ζ local basis set was used with polarization. Additional d-electrons were included in the valence electron set of Ga. Well converged spectra were obtained with a real space mesh cut-off of 250 Ryd and Monkhorst–Pack sets larger than 34 × 34 × 18 for wurtzite structures. Experimental HRTEM lattice parameters were used to build all crystal models. Atomic positions were determined by performing structural relaxations using conjugate gradient minimization of the energy, until the forces on all the atoms were smaller than 0.04 eV Å−2. In the relaxation of the models, lattice dimensions were kept constant (in accordance with the experimental values) and no constraints were imposed on the atomic positions within the supercell. To model the planar defects, defective inclusions were embedded in pristine bulk wurtzite. Eight [0001] layers of Ga–N dimers were used to separate the periodic images
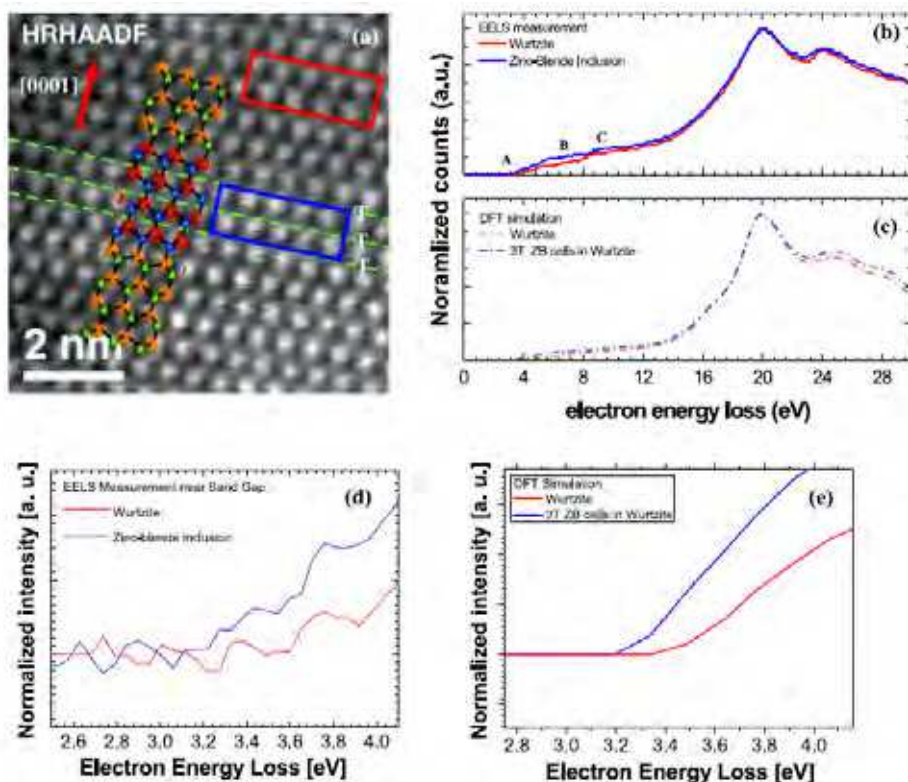
Fig. 5. High-resolution HAADF twin domain and local HREELS Bandgap analysis

of the defects. Variations in the electronic structure of less than 0.2% were observed for 16 spacing layers. The loss functions were obtained using first-order time-dependent perturbation theory to calculate the dipolar transition matrix elements between occupied and unoccupied single-electron eigenstates, as implemented in SIESTA 2.0. The optical matrix elements were calculated including the corrections due to the nonlocality of the pseudopotentials (Read & Needs, 1991), which were then used to obtain the dielectric function $\varepsilon(\omega)$ and the loss function $\text{Im}\{-1/\varepsilon(\omega)\}$ that is directly comparable with the EELS spectra. It is well known that electronic structure calculations within DFT-GGA generally underestimate the band gap of semiconductors (Jones & Gunnarsson, 1989). In this case, the calculated band gap for the pristine wurtzite phase was $E_W g(GGA) = 2.42$ eV, clearly lower than the experimental value $E_W g(exp) = (3.4 \pm 0.1)$ eV. We followed the most common procedure in the literature to circumvent this difficulty that is to apply scissor operators (Levine & Allan, 1989; Hughes & Sipe, 1996) that rigidly shift the conduction band in order to match the position of the main peak of the calculated and experimental EELS spectra (located at 20.1 eV in Figs. 5.(b) & (c)). Figs. 5.(c) & (e) show the simulated spectrum of the pristine wurtzite bulk and the local spectrum of the 3T cells embedded in wurtzite. These calculations not only reproduce the main features (A, B, C in Fig. 5.(b)) of both situations but also predict the experimental band gap change (Figs. 5.(d) & (e)). Notice that all spectra have been normalized to the maximum of the plasmon peak in Figs. 5.(b) & (c).

3. 3D reconstruction of 1D complex nanostructures by means of electron tomography

3.1 State of the art
Tomography

Tomography is a technique used to reconstruct the 3D morphology of an object from its projecting images. The mathematical principles which allow these techniques were established since the theorem made by Radon in 1917 (Radon, 1917). However, the necessary computer tools were not developed enough in order to perform the complex calculations. The necessity to obtain higher dimension structures from data series of fewer proportions is present in many scientific fields. The first real application was made by Bracewell in the area of astronomy in 1956 (Bracewell, 1956). He proposed a method to recreate a 2D map related to the microwaves emission of sun from 1D fan beam series profiles measured with a microwave telescope. The usefulness of 3D reconstructions was confirmed by 2 Nobel Prizes. The first, in 1979, was given to A. Cormack (Cormack, 1980) and G.N Hounsfield (Hounsfield, 1980). They developed the Computerized Axial Tomography, a very well known diagnosis technique. The second Nobel Prize was given to Aaron Klug in 1982 (Klug, 1982). His work was pioneer in 3D reconstructions of molecular structures through projecting images obtained with electron microscopy. In nanoscience and nanotechnology it is very well known that the shape, size, and morphology of a nano-object are very important factors, sometimes with similar relevance than the material composition in the final physical and chemical behavior. Nanostructured materials like nanowires, for example, are becoming materials of a huge importance since its physical properties dissociate in a significant way from the behavior that the same material would have in bulk. In general, the effects due to the nanostructuration start from 1 to few hundred nanometers. Several experimental characterization techniques are able to obtain 3D information at nanometric scale. One example is the atom-probe-field-ion microscopy which can be applied to conductive samples used in mass spectrometry (Humphreys, 2007). Another example would be the serial sectioning approach in which a tridimensional model is reconstructed through a series of slices. From this, we can extract images trough cryo TEM or even with an Atomic Force Mircroscopy (AFM). The major problem of these cross-sectional techniques is that they are destructive. Moreover, image formation techniques based on magnetic resonance or X-ray absorption remind restricted outside the nanoscale. It is for this reason that Electron Tomography becomes a very important tool for the structural modeling of nanometric objects. Computerized tomography is directly related with Radon theorem. The Radon transform is defined as a mapping into the so-called Radon space of a function describing a real space object, by the projection, or line integral, through that function along all possible lines (Fig. 6. Radon transform scheme). The Radon transform R can be visualized as the integration through a body D in real space f(x,y) along all possible line integrals L, with its normal at an angle to the horizontal.

$$Rf = \int_L f(x,y)ds \qquad (1)$$

Thus, given a sufficient number of projections, an inverse Radon transform of this space should reconstruct the object (Midgley & Weyland, 2003). A discrete sampling of the Radon transform is geometrically equivalent to the sampling of an experimental object by some form of transmitted signal or projection. The consequence of such equivalency is that the
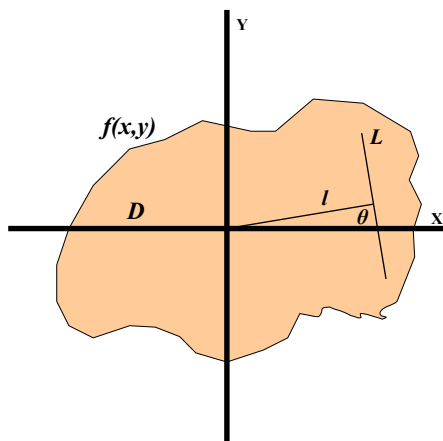
Fig. 6. Radon transform scheme

reconstruction of the structure of an object *f(x,y)* from projections *Rf* can be achieved by implementation of the inverse Radon Transform (Midgley & Weyland, 2003). In practice, the reconstruction that comes from projections is based on the knowledge between the relationship of the projections in the real space and Fourier space. The theorem of the central slice establishes that a projection of a given angle is a central section trough the Fourier transform of this object (Fig. 7. Sampling in Fourier space for tilting with equal increments). Thus, if a series of projections are acquired at different tilt angles, each projection will equate to part of an object's Fourier transform, sampling the object over the full range of frequencies in a central section.
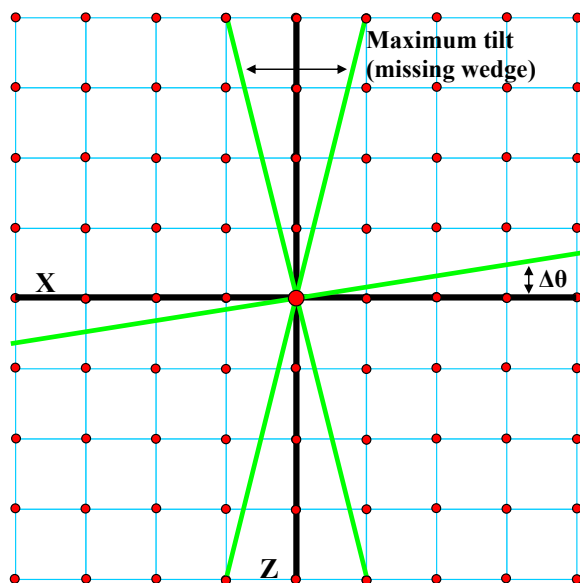

Fig. 7. Sampling in Fourier space for tilting with equal increments

Therefore tomographic reconstruction is possible from an inverse Fourier transform of the superposition of a set of Fourier transformed projections: an approach known as direct Fourier reconstruction. However, if projections are missing from an angular range, brought about by a limit on the maximum tilt angle, then Fourier space is under-sampled in those directions and as a consequence the back transform of the object will be degraded in the direction of this missing information. In this way, different sampling geometries, which are associated with the technical characteristics of the microscope sample holder and its capacity to fill the Fourier space can be used: single-axis, double-axis and conical (Penczek et al., 1995; Frank, 2006). Moreover, two problems appear in this formulation. Firstly, the projection data is always sampled at discrete angles leaving regular gaps in Fourier space. As the inverse transform requires a continuous function, radial interpolation is required to fill the gaps in Fourier space. Secondly, there is a non-uniform sampling of the data, which results in that the central zone of Fourier space has more information than the zones that are more remote. Thus, direct reconstruction methods have been replaced by the retroprojection method, which requires less compute power and allows to solve the problem of the inhomogeneities in the sampling in the Fourier space via application of some kind of filters, in general ramp filters: this method is know as Weighted BackProjection (WBP). The method of backprojection is based on inverting the set of recorded images, projecting each image back into an object space at the angle at which the original image was recorded. Using a sufficient number of backprojections, from different angles, the superposition of all the backprojected "slices" will reconstruct the original object. A schematic diagram of this approach is shown (Fig. 8. Scheme of 3D reconstruction via backprojection).
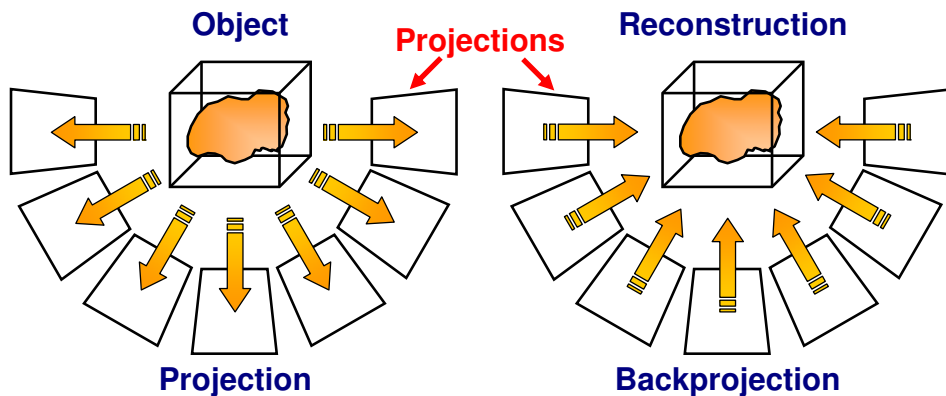

Fig. 8. Scheme of 3D reconstruction via backprojection. An object is sampled by projection from a range of angles and then reconstructed by backprojecting these projections at the original sampling angle into the object space

To provide maximum 3D information as many projections as possible should be acquired over as wide a tilt range as possible. Once we have introduced tomography fundamentals, we will focus our efforts on the electron tomography (Midgley & Weyland, 2003).

Electron tomography

The transmission electron microscope (TEM) is a very important tool in the structural and analytical characterization of objects at the nanoscale since it can offer us different sources of

information depending on the detectors that are used. However, most of the techniques that are associated with TEM are based on simple 2D projections obtained after the electron beam is transmitted through a 3D object. As it has been said before, in order to recover the tridimensional information lost with the projections we can apply some tomographic reconstruction techniques (Fig. 9. TEM tomography geometries). These techniques are widely used in the areas of medicine. Nevertheless, electronic tomography has been very little used in materials science basically for two major reasons: a) in general, inorganic materials have few 3D structure and they can be very well described by 2D projections; b) In contrast to the biology area or organic composites, tomography based on bright field (BF) images does not give accurate results as far as the crystalline samples are concerned (Weyland, 2002; Midgley et al., 2007). The explanation to this is that in order that a reconstruction can be faithful to the real object, the intensity of the projecting image must be a monotonous function of some characteristics of the real object. The amount of material projected in a parallel direction to electron beam could be a good example of this. This is known as a projection requirement. In crystalline samples, the contrast in BF conditions is ruled by the diffraction, which is related to the Bragg conditions and not necessary to the thickness of the material projected. Even all this, in the last years there has been a great effort to solve this problem by using the TEM operative mode High Angle Annular Dark Field (HAADF) (Koguchi et al., 2001; Midgley et al., 2001). Electrons scattered to low angles are predominantly coherent in nature and therefore, conventional BF and DF images exhibit sudden contrast changes depending on specimen thickness, orientation or defocus. This observation mode feature does not obey the projection requirement.
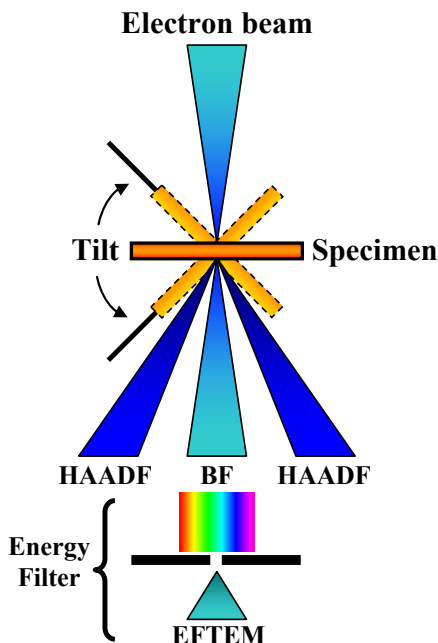

Fig. 9. Summary of the geometries of the various signals that may be used for tomographic reconstruction in TEM

However, electrons scattered to high angles are predominantly incoherent, and images formed using HAADF detector do not show the contrast changes associated with coherent scattering. Such high angle scattering is associated with electron interaction close to the nucleus of the atom and thus the cross-section for HAADF scattering approaches the unscreened Rutherford cross-section, which is strongly dependent on the atomic number Z. In practice the unscreened limit is never reached and the exact dependence depends on many factors. Nevertheless, medium-resolution STEM images formed with a HAADF detector are very sensitive to changes in specimen composition with the intensity varying monotonically with composition and specimen thickness, thus satisfying the projection requirement and giving an extra information on sample composition as it is possible to discern between different materials composing the studied reconstructed structure. For a comparison between the results obtained in crystalline samples by BF-TEM and HAADF-TEM see (Fiedrich et al., 2005). On one hand, it must be said that if HAADF gives the chance to obtain 3D structural reconstructions of crystalline nanostructures, while the Energy Filtered TEM (Möbus et al., 2003) and Electron Energy Loss Spectroscopy (van den Broek et al., 2006) have demonstrated to be a valid tool in order to find 3D compositional maps of nanostructured materials. On the other hand, the combination of HAADF with the Scanning TEM mode shows a great advantage since in scanning mode the electron dose on the surface area is time limited and then the sample damage is reduced. In the last years electron tomography has been applied to obtain solve 3D morphological and compositional problems related to nanowire synthesis. Up to our knowledge the first time that electron tomography was applied on NWs, was in 2004 to discern the growth of Metal Nanowires (Pt) inside hard template mesoporous silica (Arbiol et al., 2004a; Arbiol et al., 2004b). Lately, and thanks to the development of the HAADF STEM tomography technique, application of electron tomography to crystalline nanostructures such as nanowires has been extended. In this way, it has been applied for example to analyze the 3D morphology of core-shell GaP-GaAs NWs (Verheijen et al., 2007), the 3D structure of helical and zigzagged nanowires (Kim et al., 2008), the microsctructure of magnetic $CoFe_2O_4$ nanowires inside carbon nanotubes (Ersen et al., 2008), the 3D surface defects in core-shell nanowires (Arslan et al., 2008), the homogeneity of prismatic heterostructures on the facets of catalyst-free GaAs nanowires (Heigoldt et al., 2009), the 3D chemical arrangement on Ge-Si Nanostructures (Montoro et al., 2009) or the 3D line edge roughness in Cu NWs (Ercius et al., 2009).

3.2 Particular case: HAADF STEM tomography of coaxial multi-quantum wells in semiconductor nanowires

In order to demonstrate the capabilities of the Electron Tomography as characterization tool in the field of inorganic nanostructured crystalline materials, we have applied STEM-HAADF Tomography to coaxial nanowire heterostructures with variable quantum well thickness. In recent times the interest in III-V semiconductor nanowires has received renewed attention due to their applications in electronics and optoelectronics. The improvements of new methods of synthesis and characterization, has turned nanowires (and other nanostructures) into testers of quantum-mechanical effects (Hu et al., 2007; Shorubalko et al., 2008; Heigoldt et al., 2009). More complex structures have been obtained by combining materials coaxially and axially along the growth direction of the nanowires. Up to now, coaxial heterostructures have been considered to improve the performance of nanowire devices to confine the carriers at the core, leading to the reduction of surface

scattering (Wang et al., 2005). Core-shell structures have also been used for engineering the optoelectronical properties of the core, for example for the fabrication of multi-color light emitting diodes or lasers (Quian et al., 2008). Little attention has been paid to the geometry of the deposited shell, as the main functionality continued to be reserved to the core of the nanowire. Recently, we have shown that is possible to uniformly coat the nanowires with successive epitaxial layers resulting into multiple quantum heterostructures defining for example prismatic quantum wells (p-QW) (Morral et al., 2008b). Growth of p-QWs constitutes an additional functionality to the nanowire and, accordingly, an increased freedom design for nanostructures and devices. As a result, new architectures based in coaxial heterostructures (Fig. 10. HRTEM transversal section of AlAs-GaAs MQW nanowires grown on (001) and (111)B GaAs substrates) are being synthesized and investigated, due to their optoelectronic properties and consequent applications in the fabrication of light-emitting diodes (LEDs). Compared to bulk samples, where electrons and holes can propagate in all three dimensions, there are new effects emerging when this is no longer the case. By introducing potential barriers for these carriers one can confine them in one, two or three spatial directions. If the dimension of the confinement is of the order of the Fermi wavelength, this results into quantum confinement, ending up with carriers which can only propagate freely in less than three dimensions, speaking then of quantum wells (2D), wires (1D) or dots (0D) respectively (Wegscheider et al., 1993; Schedelbeck et al., 1997). In the example selected to illustrate the electron tomography potentiality, we used a layer sequence of $Al_{0.35}Ga_{0.55}As$, GaAs, $Al_{0.35}Ga_{0.55}As$ for building the quantum well and a final layer of GaAs to prevent oxidation of $Al_{0.35}Ga_{0.55}As$.
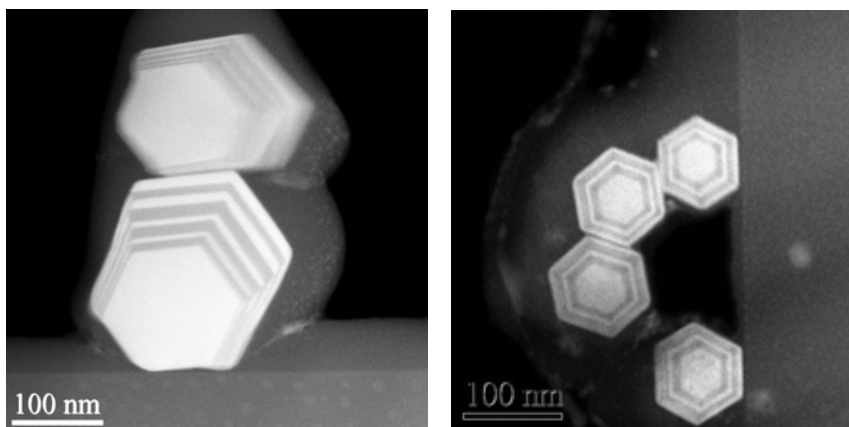

Fig. 10. HRTEM transversal section of AlAs-GaAs MQW nanowires grown on (001) and (111)B GaAs substrates, left and right, respectively

For this material combination, a type I quantum well is formed in the GaAs layer sandwiched between the $Al_{0.35}Ga_{0.55}As$ barrier layers. By varying the thickness of the QW, it is possible to control the confinement energy of the carriers. In this way the wavelength of the emitted light can be tuned, adding new functionality to the heterostructured NWs. Nanowires have been grown on a (001) and (111)B GaAs substrates by molecular beam epitaxy (MBE). The substrate was coated with a SiO_2 layer of about 10nm thick. A recent work (Morral et al., 2008a) showed that when the thickness of SiO_2 is less than 30nm an

Thank You for previewing this eBook

You can read the full version of this eBook in different formats:

- ➢ HTML (Free /Available to everyone)

- ➢ PDF / TXT (Available to V.I.P. members. Free Standard members can access up to 5 PDF/TXT eBooks per month each month)

- ➢ Epub & Mobipocket (Exclusive to V.I.P. members)

To download this full book, simply select the format you desire below